Lawrence Berkeley National Laboratory

Title
Short-range atmospheric dispersion of carbon dioxide

Permalink
https://escholarship.org/uc/item/1c9887tc

Author
Cortis, A.

Publication Date
2009-12-01

Peer reviewed

Short-range atmospheric dispersion of carbon dioxide

Andrea Cortis and Curtis M. Oldenburg

Earth Sciences Division
Lawrence Berkeley National Laboratory
One Cyclotron Rd.
Berkeley, CA 94720

Abstract—We present a numerical study aimed at quantifying the effects of concentration-dependent density on the spread of a seeping plume of CO_2 into the atmosphere such as could arise from a leaking geologic carbon sequestration site. Results of numerical models can be used to supplement field monitoring estimates of CO_2 seepage flux by modeling transport and dispersion between the source emission and concentration-measurement points. We focus on modeling CO_2 seepage dispersion over relatively short distances where density effects are likely to be important. We model dense gas dispersion using the steady-state Reynolds averaged Navier-Stokes equations with density-dependence in the gravity term. Results for a two-dimensional system show density dependence emerges at higher fluxes than prior estimates. A universal scaling relation was derived that allows estimation of flux from concentrations measured downwind and vice versa.

1 Introduction

Carbon Capture and Storage (CCS) has emerged as a technology for reducing CO_2 emissions into the atmosphere from point sources (e.g., power plants, cement plants, and oil refineries). In CCS, Captured CO_2 is stored in deep geologic formations (such as depleted oil

and gas reservoirs, and brine formations) known as Geologic Carbon Sequestration (GCS) sites. Possible seepage (escape of CO_2 from the GCS site into the atmosphere) represents a significant concern from the point of view of safety and effectiveness. In order to ensure the safety and effectiveness of GCS sites, surface monitoring networks to detect, locate, and quantify seepage, if any, are needed (Benson, 2006; Cortis et al., 2008). Understanding the dispersion processes occurring above-ground between the emission area and surface monitoring instruments is essential to interpreting measurements.

Different measurement methods for CO_2 concentration and soil fluxes exist (Oldenburg et al., 2003; Lewicki et al., 2007; Leuning et al., 2008). In order to be detectable, however, the allowed seepage flux should be larger than the average respiration flux by an amplification factor λ, a measure of the precision with which seepage flux can be distinguished from the background respiration flux (Cortis et al., 2008). According to the optimal strategies introduced by Cortis et al. (2008), monitoring costs directly depend on the value of the amplification factor; enhancing the interpretation and reliability of the measurement methods can thus significantly improve the economics of CCS projects.

While the reliability in CO_2 flux and concentration measurements depends critically on the availability of well-designed and controlled field experiments, numerical models can provide an alternative way for increasing our confidence in measured flux values. Numerical atmospheric dispersion models can significantly enhance the reliability of the various measurement methods by providing (1) predictions of plume profiles over time and space and (2) indications of measurement errors due to meteorological parameter sensitivity. Following the tragedies of the natural degassing of the Cameroonian lakes Monoun in 1984 and Nyos in 1986, and the industrial accidents in Seveso, Italy in 1976 and Bophal, India in 1984, intense research efforts have been directed towards the understanding the physics of large denser-than-air toxic plumes over significantly large distances. Thorough literature reviews can be found in the classical works of Pasquill and Smith (1983), Britter and Mc-Quaid (1998), and Arya (1999), which describe models of the evolution of dense-gas plume on distances ranging from a few hundred meters to a few kilometers.

When considering static monitoring networks for seepage detection at GCS sites, the typical spacing between Eddy Covariance Towers (ECT) is estimated to be well below the kilometer scale (Cortis et al., 2008), and short-distance models for the evolution of the CO_2 plumes need thus be considered. Despite the occurrence of small-scale accidents such as at the Idaho National Engineering and Environmental Laboratory (INEEL, 1999) where a total flood-type CO_2 fire extinguishing system discharged without warning into a room resulting in a fatality and injuries, the short-distance evolution of dense-gas plumes has received less attention in the scientific literature. Exceptions include the extensive work of Hanna and Steinberg (2001); Hanna and Chang (2001); Snyder (2001).

Extrapolation of long-distance models to short distances is often not justified, and experimental data is lacking. A coupled subsurface-atmospheric flux model was presented by Oldenburg and Unger (2004), but did not take into account the effects of variable density in the atmospheric boundary layer that is just above the ground. Macedonio and Costa (2002) proposed a model that takes into account the effects of density and seeping gas temperature, but the boundary conditions make the interpretation of their results difficult.

The aim of this work is to provide generalized results of concentration profiles of dense-gas plumes that may be used to improve on the degree of confidence that we have in field atmospheric measurements. To this end, we present a series of numerical simulations aimed at modeling the short-distance concentration profiles of dense-gas plumes subject to atmospheric dispersion. The approach is based on the coupling of incompressible, isothermal, steady-state Navier-Stokes (NS) equations for the flow, where air density and viscosity de-

pend locally on the value of the CO_2 concentration. In particular the effects of density on flow and transport are examined and both quantitative and qualitative features of this type of transport are identified, which provide guidelines and numerical tools to expedite evaluation of the quantity of interest even on a real-time, field setup.

2 Physical Model

For steady-state subsonic isothermal flows, compressible fluids (such as air at standard conditions) may be approximated as incompressible fluids, where the governing NS equations can be written as:

$$\nabla \cdot \mathbf{v} = 0 \tag{1a}$$
$$\rho(\mathbf{v} \cdot \nabla)\mathbf{v} + \nabla p - \left[\nabla \eta \left(\nabla \mathbf{v} + (\nabla \mathbf{v})^T \right) \right] = \mathbf{f} \tag{1b}$$

where p is pressure [Pa], $\mathbf{v}$ [m s^{-1}] is the fluid velocity, ρ is the density [kg m^{-3}], η is the dynamic viscosity [Pa s], and $\mathbf{f}$ represents the gravitational force (per unit volume) [N m^{-3}]. Under the incompressibility assumption, density ρ is a constant and mass conservation is represented by (1a). Atmospheric flows are generally turbulent, i.e., they are characterized by large Reynolds numbers, $Re = \rho v L / \eta$, where L is a characteristic length scale of the fully developed turbulence. As NS equations admit analytical solutions only for the most simple geometries, numerical methods of solution are needed. Two main numerical solution strategies can be identified: (i) Direct Numerical Simulations (DNS) and (ii) turbulence closure models. In DNS the flow and pressure fields' entire range of spatial and temporal scales of turbulence must be resolved in the computational mesh, from the smallest dissipative scale, up to the integral scale L. The smallest dissipative scale that needs to be considered is the so-called Kolmogorov scale $\ell = (v^3/\varepsilon^{1/4})$ and $\varepsilon \sim v'^3/L$ is the rate of kinetic energy dissipation, where v' are velocity fluctuations. With these constraints, the memory required for a DNS can be estimated on the order of $Re^{9/4}$, whereas the number of operations grows as Re^3, and the use of super-computers becomes necessary (Tu et al., 2008).

Turbulence models represent an alternative approach, in which turbulence effects are modeled on top of a spatially-averaged version of the NS equations. The key observation for this type of modeling is that at large Reynolds numbers eddy-flow structures appear at all scales of observation, down to the Kolmogorov scale where energy is dissipated into heat by viscous forces. Generally, however, when examining dispersion we are interested in averages over length and time scales much larger than almost all the eddies and all the relevant quantities can be conveniently decomposed as the sum of their mean value and a perturbation, e.g., $\mathbf{v} = \bar{\mathbf{v}} + \mathbf{v}'$. Substitution into the NS equations of these decompositions for velocity and pressure, yields the so-called Reynolds-averaged NS equations

$$\nabla \cdot \bar{\mathbf{v}} = 0 \tag{2a}$$
$$\rho(\bar{\mathbf{v}} \cdot \nabla)\bar{\mathbf{v}} + \nabla \bar{p} - \left[\nabla \eta \left(\nabla \bar{\mathbf{v}} + (\nabla \bar{\mathbf{v}})^T \right) + \nabla \left(\rho \overline{\mathbf{v}'\mathbf{v}'} \right) \right] = \mathbf{f} \tag{2b}$$

The Reynolds-averaged NS equations are structurally similar to the NS equations except for the presence of the additional stress term $\nabla \left(\overline{\rho \mathbf{v}'\mathbf{v}'} \right)$. This additional stress, often called Reynolds stress, stems from the covariance of the fluctuating velocity field $\mathbf{v}'$, the effects of which can be modeled as a macroscopic turbulent viscosity η_T

$$\rho \overline{\mathbf{v}'\mathbf{v}'} - \frac{\rho}{3} trace(\overline{\mathbf{v}'\mathbf{v}'}) \mathsf{I} = \eta_T \left(\nabla \bar{\mathbf{v}} + (\nabla \bar{\mathbf{v}}) \right)^T \tag{3}$$

The introduction of the turbulent viscosity leads thus to the following form of the Reynolds averaged NS equations:

$$\nabla \cdot \overline{\mathbf{v}} = 0 \tag{4a}$$

$$\rho(\overline{\mathbf{v}} \cdot \nabla)\overline{\mathbf{v}} + \nabla \overline{p} - \left[\nabla(\eta + \eta_T)\left(\nabla \overline{\mathbf{v}} + (\nabla \overline{\mathbf{v}})^T\right)\right] = \mathbf{f} \tag{4b}$$

where the term $\frac{\rho}{3} trace(\overline{\mathbf{v}'\mathbf{v}'})\mathbf{I}$ has been added to the mean pressure $\overline{p}$. The problem is now shifted to finding an estimate of η, and for this we need additional closure equations. In this work, we make use of the so-called $k - \varepsilon$ model, which requires the introduction of a set of two coupled PDEs for the kinetic energy $k = \frac{1}{2}\overline{v_i v_i}$, and the dissipation rate of turbulent energy ε (Stull, 1988)

$$\rho\frac{\partial k}{\partial t} - \nabla \cdot \left[\left(\eta + \rho\frac{C_\eta}{\sigma_k}\frac{k^2}{\varepsilon}\right)\nabla k\right] + \rho\overline{\mathbf{v}} \cdot \nabla k = \rho C_\eta \frac{k^2}{2\varepsilon}\left(\nabla \overline{\mathbf{v}} + (\nabla \overline{\mathbf{v}})^T\right)^2 - \rho\varepsilon, \tag{5a}$$

$$\rho\frac{\partial \varepsilon}{\partial t} - \nabla \cdot \left[\left(\eta + \rho\frac{C_\eta}{\sigma_\varepsilon}\frac{k^2}{\varepsilon}\right)\nabla \varepsilon\right] + \rho\overline{\mathbf{v}} \cdot \nabla \varepsilon = \rho C_{\varepsilon 1}\frac{k}{2}\left(\nabla \overline{\mathbf{v}} + (\nabla \overline{\mathbf{v}})^T\right)^2 - \rho C_{\varepsilon 1}\frac{\varepsilon^2}{k}. \tag{5b}$$

where, $C_\eta = 0.09$, $C_{\varepsilon 1} = 1.44$, $C_{\varepsilon 2} = 1.92$, $\sigma_k = 0.9$, and $\sigma_\varepsilon = 1.3$ are empirical constants determined from experimental data. The turbulent viscosity is then modeled as $\eta_T = \rho C_\eta \frac{k^2}{\varepsilon}$ (Stull, 1988). Boundary conditions for k and ε must be specified to complete the description of the physical model. This is often difficult and a source of uncertainty since the incoming turbulence is rarely known exactly, and an educated guess of the incoming turbulence is required. Equations 4 together with 5 represent a complete model of the turbulent flow.

In this work, however, our interest rests mainly on the density effects of a dense-gas plume on the flow, and the subsequent plume dispersion. When the concentration of CO_2 becomes sufficiently large, the variations of the density and viscosity with respect to the standard atmospheric composition become significant and affect the overall characteristics of the flow. We propose a model where density and viscosity can be calculated by means of constitutive laws as a function of the CO_2 molar concentration (Reagan, 2008; Moridis et al., 2008). The limit values for the density are $\rho_a = 1.18$ and $\rho_c = 1.82$ [kg m^{-3}], for air and pure CO_2, respectively, whereas the limit values for the viscosity are $\eta_a = 1.807 \times 10^{-5}$ and $\eta_c = 1.461 \times 10^{-5}$. All these values are considered at constant temperature $T = 295$ K.

At steady-state conditions, the CO_2 concentration spatial distribution $c = c(x, y, z)$ induces spatially varying density $\rho = \rho(x, y, z)$ and viscosity $\eta = \eta(x, y, z)$ fields that are accounted for in the incompressible NS equations.

Atmospheric dispersion is often treated by means of a Fickian hypothesis on the flux of the contaminant, i.e., by modeling the concentration flux of the contaminant as proportional to the gradient of the concentration and the proportionality constant is the molecular diffusivity. This is a well known picture of transport that leads to the classical advection-dispersion equation (ADE)

$$\frac{\partial c}{\partial t} = -\mathbf{v} \cdot \nabla c + \nabla(D\nabla c). \tag{6}$$

According to the ADE description in eq. (6), the trace gas is advected along the flow streamlines and further dispersed across neighboring streamlines by Brownian motion effects. While the ADE with molecular diffusion can be seen as an appropriate way to describe transport at extremely small scales and more or less homogeneous velocity fields, doubts can be raised about the appropriateness of its use at larger scales, where the effects of the turbulence at all scales accumulate. In this work we will consider only the steady-state picture of transport, hence $\frac{\partial c}{\partial t} = 0$. The ADE picture of transport has undergone much scrutiny

when contaminant transport in heterogeneous geological media is considered. For this specific application, it is now recognized that even small heterogeneity in the flow path can significantly affect macroscopic transport properties giving rise to so-called macro (scale-dependent) dispersion coefficients. This picture presents striking analogies to the case of atmospheric turbulence, where energy is transferred from larger to smaller eddies, leading ultimately to dissipation by viscosity. In other words, a contaminant transported in the atmosphere experiences a whole host of different fluctuating velocities $\mathbf{v}'$ that accumulate into apparent macroscopic scale-dependent dispersion coefficients (see, e.g., Berkowitz et al., 2006, and refs. therein). This explains the difference in the order of magnitude between the molecular diffusion coefficient, which is on the order of 10^{-5} $m^2 s^{-1}$ and dispersion coefficients fitted to field experiments, which are reported to be five to six orders of magnitude larger. A regrettable paucity in well-constrained experimental data and solid theoretical explanations for the macroscopic transport behavior of a contaminant in the atmosphere at 10^2 m scale forces us to adopt a constitutive law for the dispersion coefficient that reflects both the details of the computations and is consistent with apparent dispersion measurements (see, e.g., Davis et al., 1986). Specifically we will assume that the dispersion coefficient in the ADE is locally (i.e., for each point in space) equal to $D = f \eta_T / \rho$, where $f \sim 10 - 100$. The range for f was obtained by estimating numerically the average values of η_T for different flow conditions to make the value of D consistent with values of the apparent dispersion coefficient on the order of $1 - 5$ m^2 s^{-1} reported for field conditions at sub-km scales.

3 Numerical Model

The coupled system of equations defined by the Reynolds-Averaged NS equations (2), the $k - \varepsilon$ closure equations (5), the advection-dispersion equation (6), augmented by the constitutive equations for $\rho = \rho(c)$, $\eta = \eta(c)$, the phenomenological expression for the dispersion coefficient, and the appropriate boundary conditions, is solved by means of a finite element scheme and implemented in the commercial software COMSOL Multiphysics v3.4 (COMSOL, 2008).

In this work, we confine ourselves to model the steady-state concentration profile of a seeping dense-gas plume in a two-dimensional vertical section of the lower atmosphere as depicted in Figure 1. A seeping zone of width b [m] is located at a distance a from the inlet region (left-hand side of the rectangular computational domain). A logarithmic, no-slip surface ($\frac{\partial v}{\partial z} = 0$, at $z = 0$) profile for the wind velocity v [m s^{-1}] is imposed at the left of the domain. A no-flux boundary condition for the wind velocity is imposed at the top of the computational domain, whereas surface roughness conditions are imposed at the bottom. The CO_2 gas seepage is modeled by imposing a flux boundary condition on the seeping region of width b. At the right-hand side of the computational domain we impose a free-flux (Neumann) boundary condition allowing for outflow.

The computational domain is discretized with triangular elements (see Figure 2), and the mesh density is denser near the seepage region to increase numerical accuracy. The elements used for the fluid flow are Lagrange P2-P1 elements (quadratic and linear approximation for the velocity components and pressure, respectively). The concentration is discretized by means of Lagrange-quadratic elements. The number of elements was 7064, for a total of 75,586 degrees of freedom. For the numerical solution of the fully-coupled system of equations, we used the Pardiso solver (http://www.pardiso-project.org/) as implemented in the COMSOL Multiphysics software.

The final set of equations is highly non-linear, and tends to be particularly stiff for low wind speeds and large density contrast. For this reason, we adopted a step-by-step approach to the solution. Given a wind speed, the solution for a higher wind speed was obtained, which was subsequently used as the initial solution for a problem with a lower wind speed. This parametric approach allowed us to achieve convergence for relatively low values of the wind speed. The tolerance for the iterative residual of the system was set equal to 10^{-4} to ensure convergence.

We have validated the numerical solutions obtained with our code against an analytical solution valid for passive (no density dependence) transport. The reference analytical solution assumes passive tracer Gaussian dispersion, with constant wind profile, and can be approximated by the expression (Arya, 1999, eq. 6.45)

$$c(x,z) = \frac{\int_{-\infty}^{+\infty} c(x=+\infty,z)\,dz}{\sqrt{4\pi v(z)Dx}} \exp\left(-\frac{vz^2}{4Dx}\right) \tag{7}$$

Equation (7) is valid at a sufficiently large distance from the injection point. We considered the case of constant velocity $v = 1$ m s^{-1} and dispersion coefficient $D = 2$ m s^{-2}. The comparison is presented in Figure 3 The agreement between numerical and analytical solutions is satisfactory at a sufficiently large distance from the injections point, as expected by the assumptions on the analytical solution (7). The difference between the two concentration profiles can be ascribed to the different boundary condition for the seepage: imposed flux in our model vs imposed concentration in (7).

4 Results

The relative importance of the density effects on plume dispersion can be characterized by the so-called global Richardson number,

$$Ri^\star = \frac{g_0' q_0}{bU^3}, \tag{8}$$

where q_0 is the volumetric seepage flow rate [m^3 s^{-1}], b is the seepage width [m], U is the wind velocity [m s^{-1}] at the reference altitude $z = 10$ m, and $g_0' = g\frac{\rho_c - \rho_a}{\rho_a}$, is the reduced gravity. According to Britter and McQuaid (1998), the transition between passive and density-driven transport occurs at $(Ri^\star)^{\frac{1}{3}} = Ri < 0.15$.

We have performed a series of numerical simulations corresponding to different values of the seepage width b [m], the wind speed v [m s^{-1}], and CO$_2$ seepage flux, Φ [mol m^{-2} s^{-1}]. The size of the 2D computational domain for all cases is $L = 50$ m, $H = 30$ m.

Figure 4 illustrates this transition threshold graphically for the two limiting values of the seepage length used in this study, i.e., $b=1$ and $b=6$. Our computations cover both the active and passive cases. The reduced Richardson number corresponding to our numerical computations ranges from very low values to a maximum of $Ri \sim 2$.

Figure 5 illustrates a typical simulation for a flux $\Phi = 32\mu$mol m^{-2} s^{-1}, values of $a = 5$ m, $b = 2$ m, and wind speed at $z = 3$ m equal to 0.5 m s^{-1}. Only a 20×10 inset of the 520×30 computational domain is shown. In this case, the value of the CO$_2$ concentration is smaller than 1 ppmv, a value too low to significantly modify the values of density and viscosity of the air. This can be seen by looking at the wind streamlines which are evidently parallel to the ground surface (unperturbed).

Figure 6 illustrates the effect of the increase in the value of the CO_2 flux, which is now 10^6 times larger. The maximum value of the concentration is now on the order of 4×10^5 ppmv, a value sufficiently large to significantly modify the values of density and viscosity of the air. This effect can now be appreciated by looking at the wind streamlines, which now bend in the region around the seepage area. A significant recirculation area can be identified over the seepage area: the streamlines recirculate the CO2, increasing the concentration buildup and enhancing the upwind tail of the concentration profile.

For intermediate values of the seepage flux between the two extreme cases presented in Figures 5 and 6, we can find a transition region in which the streamlines are perturbed over the seepage area, but no recirculation region is present; this transition will be analyzed in more detail later.

Figure 7 summarizes the concentration profiles for the case $b = 6$ m and $a = 5$ m. The distance x [m] is measured from the downwind edge of the seepage area, and the concentration $c(x)$ at ground level ($z = 0$) is expressed in units of mol m^{-3}. The flux Φ ranges between 2×10^{-5} and 1.8×10^1 μmol m^{-2} s^{-1}, and four different wind velocities at $z = 3$ m have been considered, namely $v = 0.84, 0.42, 1.26$, and 1.68 m s^{-1}, respectively.

The results presented in Figure 7 suggest the introduction of a non-dimensional concentration $\xi = vc/\Phi$. Figure 8 plots the non-dimensional ground-level concentration profiles. Most of the profiles collapse now on a single universal curve. Some outliers can be observed for relatively high values of the CO_2 flux, and for lower values of the wind speed. This suggests the existence of a universal scaling for the nondimensional concentration. Figure 9 summarizes all the profiles of Figure 8 (the outliers have been omitted from this plot). There is clearly a universal scaling of the ground level concentration profiles as a function of the seepage flux and wind velocity, and the solid line in Figure 9 represents the best fit model,

$$\log(\xi(x)) = \sum_{k=0}^{4} \alpha_k \log^k(x) \tag{9}$$

where log represents the base 10 logarithm. The coefficients α_k of the universal scaling obviously depend on the value of the seepage width b. This universal scaling persists also as a function of the elevation z at which the concentration is measured up to $z \sim 5$ m and then it starts to bifurcate into two stable regimes. This behavior is illustrated in Figure 10, where the color of each curve represents the value of the Richardson number Ri of each profile. We find that the threshold between passive and density-dominated regimes appears around the value $Ri \sim 0.5$, significantly larger value than the 0.15 suggested by Britter and McQuaid (1988). The scaling proposed in (9) is consistent with the wind-tunnel near-ground concentration profile measurements presented in Snyder (2001).

In Figure 11, we classify the same numerical results presented in Figure 10 according to a different scheme. While the Richardson number is an a priori analysis of the influence of density on dispersion, Figure 11 presents an a posteriori analysis based on the observation of recirculation zones near the seepage area. The concentration profiles in red are those that exhibit recirculation, i.e., closed-loop streamlines. It can be seen that the transition to recirculation-dominated flow happens around $Ri \sim 1$. This means that we can identify a interval of Richardson numbers $Ri \sim [0.7 - 1.0]$ that characterizes the transition from purely passive to recirculation-dominated, in which density effects are present and manifest themselves by the bulging of the otherwise parallel wind streamlines. The number of configurations in the density-driven regime are, however, clearly insufficient to make any significant statistics and this observation needs further exploration before any general conclusion may be drawn.

Finally, Figure (12) shows the average concentration profiles at different elevations z, for the case $b = 6$ m where the recirculating zone cases have been eliminated. Similar figures have been obtained for the cases $b = 1, 2, 3, 4,$ and 5 m. From the profiles, we can derive now the expressions for the coefficients α_k, and we can interpolate the coefficients as a function of z, by means of 5th order degree polynomials,

$$\alpha_k(z) = \sum_{j=0}^{j} \beta_{jk} z^j \qquad (10)$$

as illustrated in Figure 13. The interpolating coefficients β_{jk} are given in Table 1 as a function of the seepage width b. For intermediate values of the seepage width b, we suggest a simple linear interpolation of the coefficients.

By means of the coefficients tabulated in Table 1, we are now in the position of being able to estimate the value of the CO_2 seepage flux Φ, given a series of CO_2 concentration measurements at various elevations z, a measured value of the wind velocity v, and an estimated seepage width b, without resorting to laborious numerical solutions. This means that a technician in the field can give an estimate of the seepage flux with operations that can be easily implemented on a pocket calculator. For example, consider the case of a large-scale GCS site at which monitoring and detection methods (Oldenburg et al., 2003; Lewicki et al., 2007; Leuning et al., 2008, e.g.,) had identified the presence of anomalous CO_2 in an area and more detailed investigation (Cortis et al., 2008, e.g.,) had pinpointed an elongated seepage area (e.g., along a fault trace, or crack(s) in a paved surface). A field technician could carry out an inexpensive survey over the course of an afternoon using (1) an anemometer set up when the wind is generally transverse to the fault, and (2) a hand-held CO_2 infra red (IR) detector to measure CO_2 concentration at ground level along 10-50 m transects over the suspected seepage area. Repeated transects in a grid pattern that would presumably produce a peak concentrations near the seepage area, rapid decline in concentration upwind of the seepage area (allowing estimation of the seepage area width, b), and more gentle decline in concentration downwind of the seepage area consistent with dilution due to turbulent mixing and dispersion. Without recourse to any numerical computation, the concentration and wind velocity data could be suitably averaged and combined with the α_k parameters from Table 1 to solve for the estimate flux Φ.

More complex estimation schemes can be devised, which involve the solution of overdetermined linear systems of equations, should a sufficiently large number of measurements at different elevations z, and distances x be available. It is important to note here that the implicit assumptions used to calculate the concentration profiles (e.g., 2D vs 3D profiles, multiplier of the dispersion coefficient f, topographic conditions), may be relaxed and new interpolation functions be deduced from the corresponding numerical computations.

5 Conclusions

We have presented a numerical study aimed at understanding the effects of density on the transport behavior of CO_2 plumes seeping out of the ground. The model is aimed at improving the confidence in seepage flux field measurement values, a crucial step in providing better constraints for the optimization of monitoring networks, and thereby minimizing their costs. We simulated small-scale atmospheric flows by means of a k-ε turbulence model of the NS equations, where the density and viscosity depend on the local CO_2 concentration value. We have identified a transition region for the Richardson number that leads to a

density-dominated regime, and illustrated its effects on the contaminant transport. By defining a non-dimensional concentration normalized with respect to the value of wind velocity and seepage flux, we have identified a universal scaling for the concentration profiles, which breaks down only at extremely high values of the flux, or low values of the wind speed. The combination of such large CO_2 fluxes and no-wind conditions that lead to recirculation zones, i.e., closed loop streamlines of the wind velocity field, while extremely important from a safety and risk-assessment perspective, is unlikely to be found in the ordinary operation of a monitoring network, and urgent responses are needed instead (Cortis et al., 2008). Based on our numerical simulations, we provided simple interpolation formulas that can be used in the field to estimate seepage fluxes, given other atmospheric concentration measurements, and the measurement of the wind velocity. Numerical simulations aimed at relaxing the initial model assumptions used in this work will make it possible to extend this simple interpolation scheme and generalize it to less idealized field situations.

References

Arya S (1999) Air Pollution Meteorology and Dispersion. Oxford University Press

Benson S (2006) Monitoring carbon dioxide sequestration in deep geological formations for inventory verification and carbon credit. In: SPE-102833, 2006 Annual Technical Conference and Exhibition, Society of Petroleum Engineers, San Antonio, TX, September 2427.

Berkowitz B, Cortis A, Dentz M, Scher H (2006) Modeling non-fickian transport in geological formations as a continuous time random walk. Reviews of Geophysics 44:1–49

Britter RE, McQuaid J (1998) Workbook on the dispersion of dense gases. Contract Research Report 17/1988, Health and Safety Executive, Sheffield, UK

COMSOL (2008) Multiphysics User's Guide. COMSOL AB, v3.4 edn

Cortis A, Oldenburg CM, Benson SM (2008) The role of optimality in characterizing CO_2 seepage from geologic carbon sequestration sites. International Journal of Greenhouse Gas Control 2(4):640–652

Davis P, Reimer A, Sakiyama S, slawson P (1986) Short-range atmospheric dispersion over a heterogeneous surface–i. lateral dispersion. Atmospheric Environment (1967) 20(1):41 – 50, DOI DOI: 10.1016/0004-6981(86)90205-2

Hanna S, Chang J (2001) Use of the kit fox field data to analyze dense gas dispersion modeling issues. Atmospheric Environment 35:2231–2242

Hanna S, Steinberg K (2001) Overview of petroleum research forum (perf) dense gas dispersion modeling project. Atmospheric Environment 35:2223–2229

INEEL (1999) Supplemental response to the type a accident investigation board report of the july 28, 1998, fatality and multiple injuries resulting from release of carbon dioxide at building 648, test reactor area, idaho national engineering and environmental laboratory. Tech. Rep. INEEL/EXT-99-00282, Idaho National Engineering and Environmental Laboratory

Leuning R, Etheridge D, Luhar A, Dunse B (2008) Atmospheric monitoring and verification technologies for CO_2 geosequestration. International Journal of Greenhouse Gas Control

2(3):401 – 414, DOI DOI: 10.1016/j.ijggc.2008.01.002, eGU General Assembly 2007: Advances in CO_2 Storage in Geological Systems - EGU (2007)

Lewicki J, Oldenburg C, Dobeck L, Spangler L (2007) Surface CO_2 leakage during two shallow subsurface CO_2 releases. Geophysical Research Letters 34:L24,402, DOI 101029/2007GL032047

Macedonio G, Costa A (2002) Finite element modeling of gas dispersion in the atmosphere. In: Buccianti A, Marini L, Ottonello G, Vasell O (eds) Proceedings of the Arezzo Seminar in Fluids Geochemistry, Pacini Editore, Ospedaletto (Pisa), pp 147–159

Moridis G, Kowalsky M, , Pruess K (2008) Tough+hydrate v1.0 users manual: A code for the simulation of system behavior in hydrate-bearing geologic media. Report LBNL-0149E, Lawrence Berkeley National Laboratory

Oldenburg C, Lewicki J, Hepple R (2003) Nearsurface monitoring strategies for geologic carbon dioxide storage verification. Report LBNL-54089, Lawrence Berkeley National Laboratory

Oldenburg CM, Unger AJA (2004) Coupled vadoze zone and atmospheric surface-layer transport of carbon dioxide from geologic carbon sequestration sites. Vadose Zone Journal 3:3848–3857

Pasquill F, Smith FB (1983) Atmospheric Diffusion, 3rd edn. Ellis Horwood

Reagan M (2008) Webgaseos online application v1.0. Report LBNL/PUB-3188, Lawrence Berkeley National Laboratory, URL http://lnx.lbl.gov/gaseos/

Snyder W (2001) Wind-tunnel study of entrainment in two-dimensional dense-gas plumes at the eps's fluid modeling facility. Atmospheric Environment 35:2285–2304

Stull R (1988) An Introduction to Boundary Layer Meteorology. Kluwer Academic Publishers

Tu J, Yeoh GH, Liu C (2008) Computational Fluid Dynamics: A Practical Approach. Butterworth-Heinemann
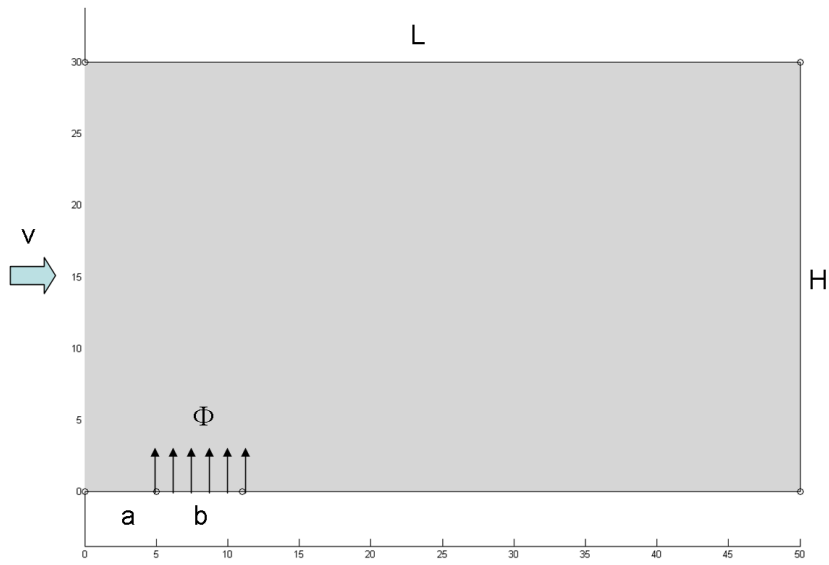
Fig. 1 Sketch of the 2D computational domain (units of [m]). Wind direction is from left to right. A seepage CO_2 flux, Φ, is imposed over region of width b at the bottom.
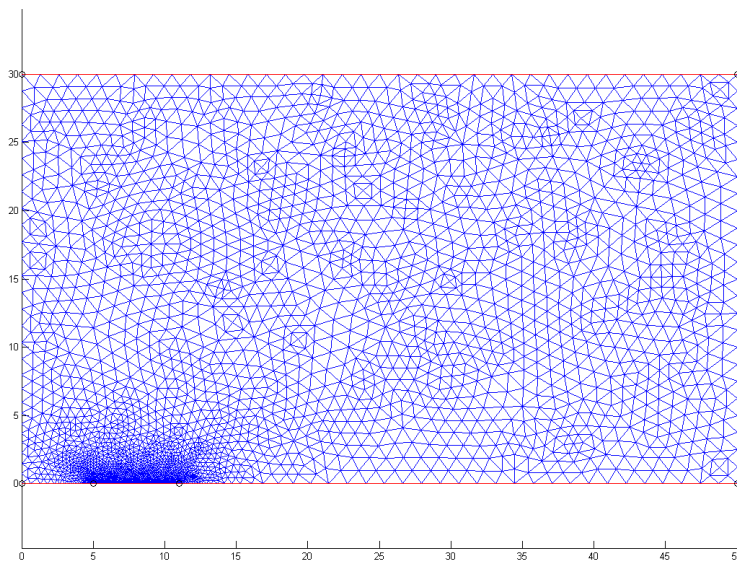

Fig. 2 Typical mesh used for the finite element simulations of density-dependent atmospheric flow and dense-gas transport (units of [m]). The higher density of the mesh corresponds to the seepage zone.

Table 1 Table of interpolation coefficients for the normalized concentration as a function of the elevation z [m], and the seepage length b [m].

b=1	z^5	z^4	z^3	z^2	z^1	z^0
α_1	-2.51×10^{-5}	9.53×10^{-4}	-1.46×10^{-2}	1.09×10^{-1}	-3.55×10^{-1}	2.84×10^{-1}
α_2	2.83×10^{-4}	-1.09×10^{-2}	1.70×10^{-1}	-1.30	4.35	-3.55
α_3	-1.16×10^{-3}	4.57×10^{-2}	-7.24×10^{-1}	5.67	-1.97×10^1	1.66×10^1
α_4	2.03×10^{-3}	-8.19×10^{-2}	1.33	-1.08×10^1	3.91×10^1	-3.48×10^1
α_5	-1.27×10^{-3}	5.28×10^{-2}	-8.87×10^{-1}	7.41	-2.86×10^1	2.57×10^1

b=2	z^5	z^4	z^3	z^2	z^1	z^0
α_1	-4.36×10^{-6}	3.26×10^{-4}	-7.65×10^{-3}	7.73×10^{-2}	-3.13×10^{-1}	2.96×10^{-1}
α_2	3.48×10^{-5}	-3.42×10^{-3}	8.76×10^{-2}	-9.28×10^{-1}	3.90	-3.77
α_3	-6.23×10^{-5}	1.25×10^{-2}	-3.64×10^{-1}	4.09	-1.80×10^1	1.80×10^1
α_4	-9.14×10^{-5}	-1.81×10^{-2}	6.45×10^{-1}	-7.82	3.65×10^1	-3.85×10^1
α_5	2.44×10^{-4}	7.52×10^{-3}	-4.04×10^{-1}	5.42	-2.74×10^1	3.00×10^1

b=3	z^5	z^4	z^3	z^2	z^1	z^0
α_1	-2.86×10^{-6}	2.56×10^{-4}	-6.82×10^{-3}	7.81×10^{-2}	-3.60×10^{-1}	4.05×10^{-1}
α_2	2.11×10^{-5}	-2.74×10^{-3}	8.05×10^{-2}	-9.68×10^{-1}	4.62	-5.29
α_3	-2.25×10^{-5}	1.03×10^{-2}	-3.47×10^{-1}	4.43	-2.20×10^1	2.59×10^1
α_4	-1.22×10^{-4}	-1.55×10^{-2}	6.44×10^{-1}	-8.83	4.64×10^1	-5.70×10^1
α_5	2.29×10^{-4}	7.05×10^{-3}	-4.30×10^{-1}	6.45	-3.63×10^1	4.67×10^1

b=4	z^5	z^4	z^3	z^2	z^1	z^0
α_1	-2.86×10^{-6}	2.56×10^{-4}	-6.82×10^{-3}	7.81×10^{-2}	-3.60×10^{-1}	4.05×10^{-1}
α_2	2.11×10^{-5}	-2.74×10^{-3}	8.05×10^{-2}	-9.68×10^{-1}	4.62	-5.29
α_3	-2.25×10^{-5}	1.03×10^{-2}	-3.47×10^{-1}	4.43	-2.20×10^1	2.59×10^1
α_4	-1.22×10^{-4}	-1.55×10^{-2}	6.44×10^{-1}	-8.83	4.64×10^1	-5.70×10^1
α_5	2.29×10^{-4}	7.05×10^{-3}	-4.30×10^{-1}	6.45	-3.63×10^1	4.67×10^1

b=5	z^5	z^4	z^3	z^2	z^1	z^0
α_1	-6.25×10^{-6}	3.66×10^{-4}	-8.38×10^{-3}	9.08×10^{-2}	-4.16×10^{-1}	4.85×10^{-1}
α_2	6.54×10^{-5}	-4.20×10^{-3}	1.02×10^{-1}	-1.14	5.40	-6.40
α_3	-2.38×10^{-4}	1.75×10^{-2}	-4.53×10^{-1}	5.33	-2.62×10^1	3.17×10^1
α_4	3.38×10^{-4}	-3.11×10^{-2}	8.79×10^{-1}	-1.09×10^1	5.59×10^1	-7.03×10^1
α_5	-1.34×10^{-4}	1.96×10^{-2}	-6.22×10^{-1}	8.17	-4.44×10^1	5.85×10^1

b=6	z^5	z^4	z^3	z^2	z^1	z^0
α_1	-3.04×10^{-5}	1.07×10^{-3}	-1.56×10^{-2}	1.25×10^{-1}	-5.05×10^{-1}	5.93×10^{-1}
α_2	3.66×10^{-4}	-1.32×10^{-2}	1.98×10^{-1}	-1.61	6.66	-7.91
α_3	-1.59×10^{-3}	5.98×10^{-2}	-9.25×10^{-1}	7.72	-3.28×10^1	3.95×10^1
α_4	2.92×10^{-3}	-1.17×10^{-1}	1.89	-1.67×10^1	7.12×10^1	-8.85×10^1
α_5	-1.80×10^{-3}	8.06×10^{-2}	-1.41	1.27×10^1	-5.77×10^1	7.45×10^1
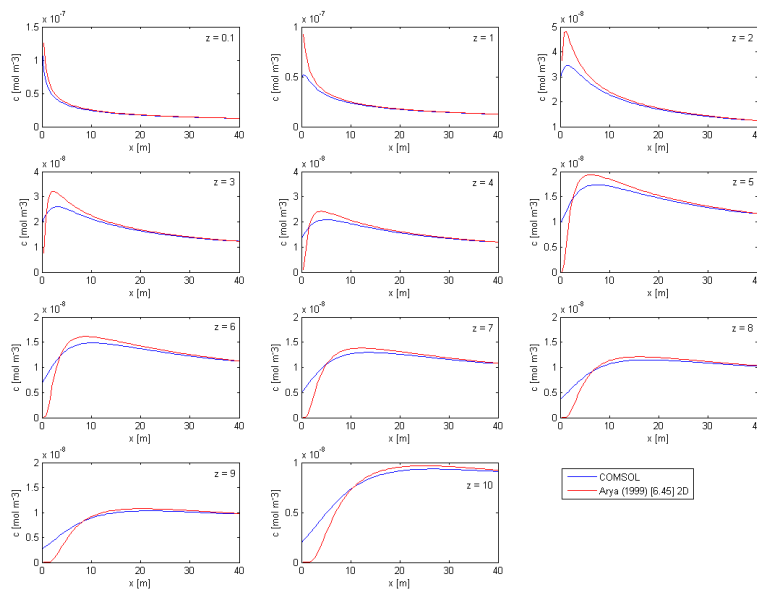
Fig. 3 Validation of the numerical model for the case of a non-dense tracer gas. In blue the solution of our numerical model, and in red the ADE solution in (7). The difference between the two concentration profiles can be ascribed to the different boundary condition for the seepage: imposed flux in our model vs imposed concentration in the ADE model.
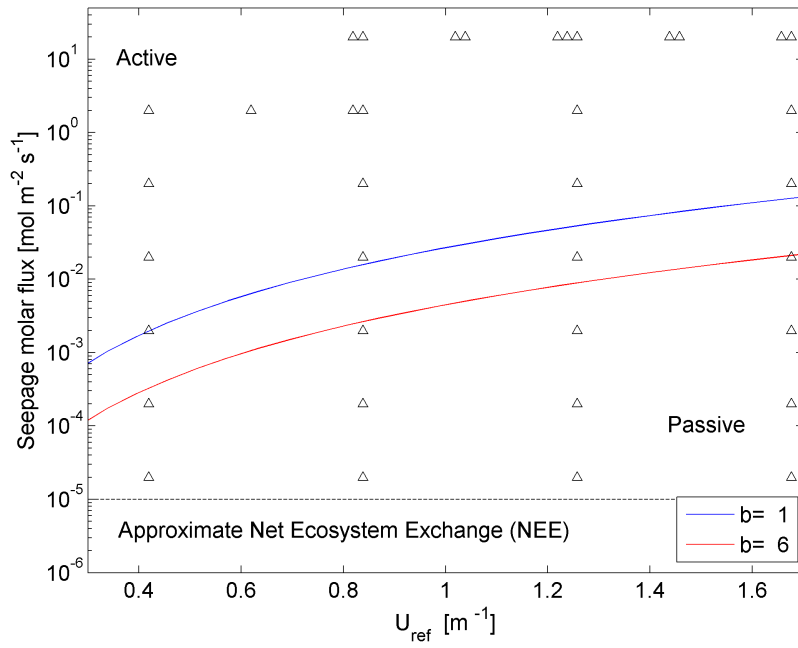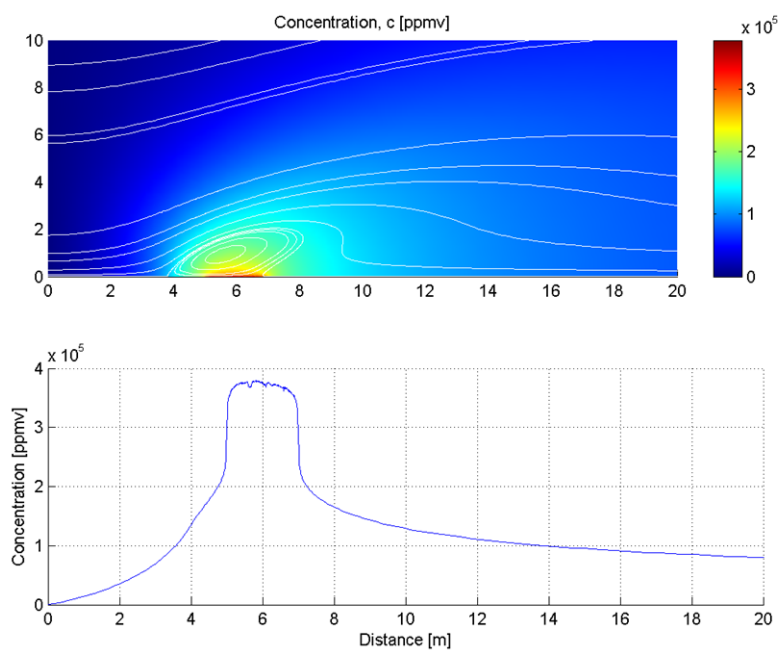
Fig. 4 Summary of the reference velocity values U_{ref} (estimated at the edge of the seepage area and at an elevation $z = 10$ m) and seepage fluxes for the range of situations explored in this work. The black dashed line represents an approximate estimate of the Net Ecosystem Exchange (NEE). Triangles represent the configurations investigated in this study.
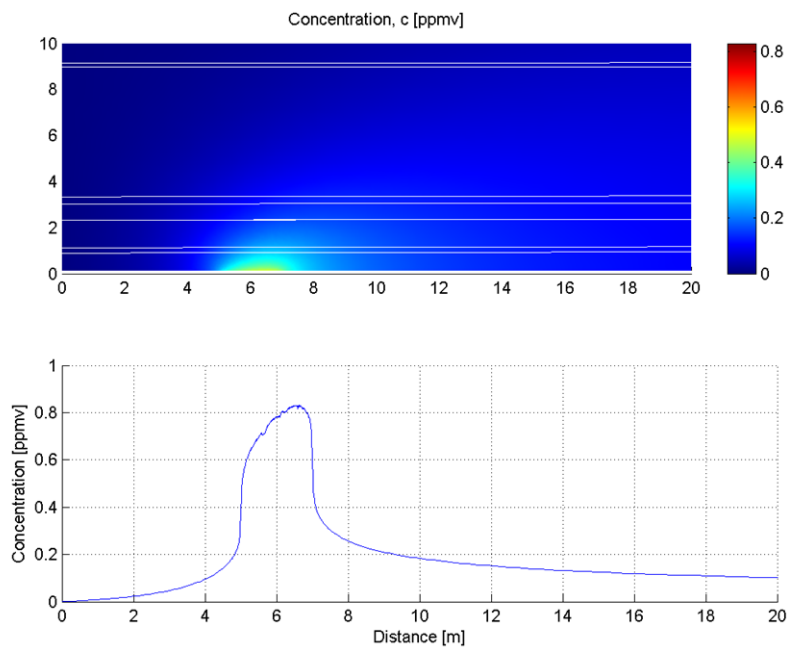
Fig. 5 Concentration map and profile at ground level for a 32 μmol m^{-2} s^{-1} CO$_2$ seepage flux.

Fig. 6 Concentration map and profile at ground level for a 32 mol m^{-2} s^{-1} CO_2 seepage flux.
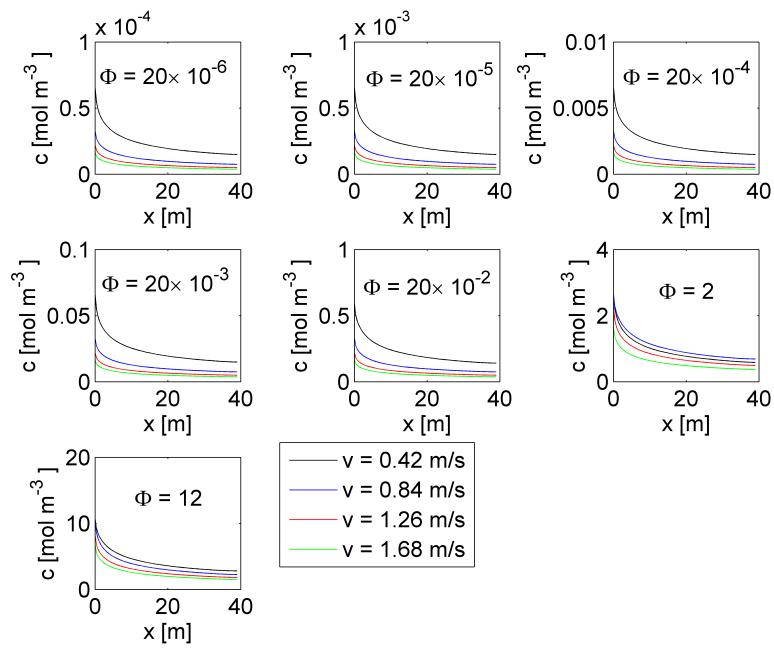
Fig. 7 Concentration profiles at ground level for different level of the seepage flux Φ μmol m^{-2} s^{-1} and for different wind velocities. The black, blue, red, and green curves correspond to assigned wind velocities at $z = 3$ m equal to $v = 0.42, 0.84, 1.26, 1.68$ m s^{-1}, respectively. The seepage width $b = 6$ m.
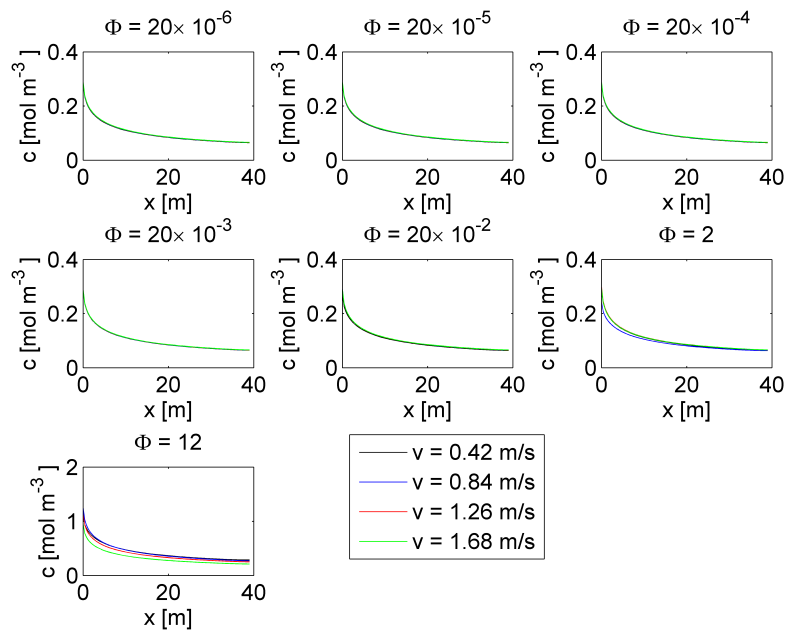
Fig. 8 Normalized concentration profiles at ground level for the case $b = 6$ m. Deviations from a universal scaling can be observed for relatively high values of the CO_2 flux, and for lower values of the wind speed.
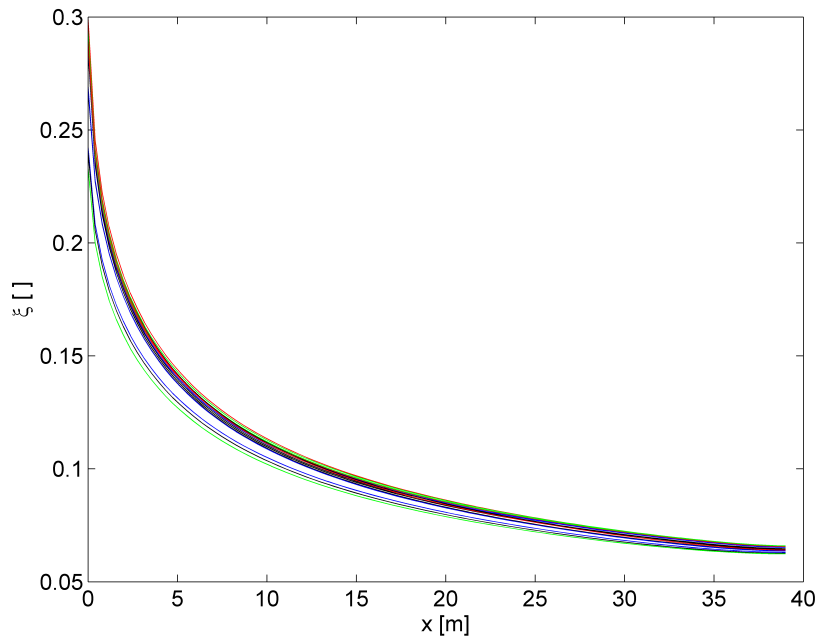
Fig. 9 Universal scaling of the concentration profiles at ground level for different levels of the seepage flux and for different wind velocity for the case of a seepage area that extends linearly for $b = 6$ m.
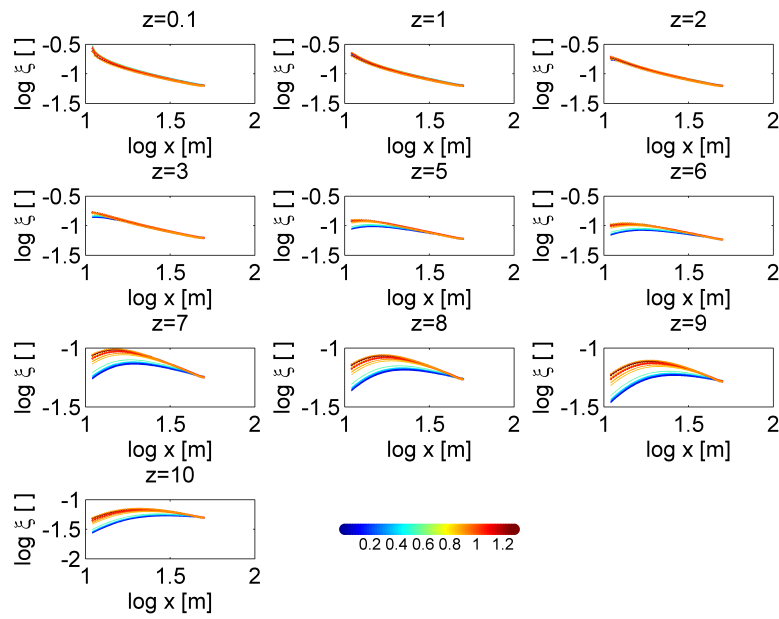
Fig. 10 Normalized concentration profile at various elevations *z*, for the case $b = 6$. Colors indicate the value of the cubic root of the Richardson number. According to Britter and McQuaid (1998), values larger than 0.15 should indicate density effects on transport. Our numerical simulations seem to indicate a threshold around $Ri \sim 0.5$.
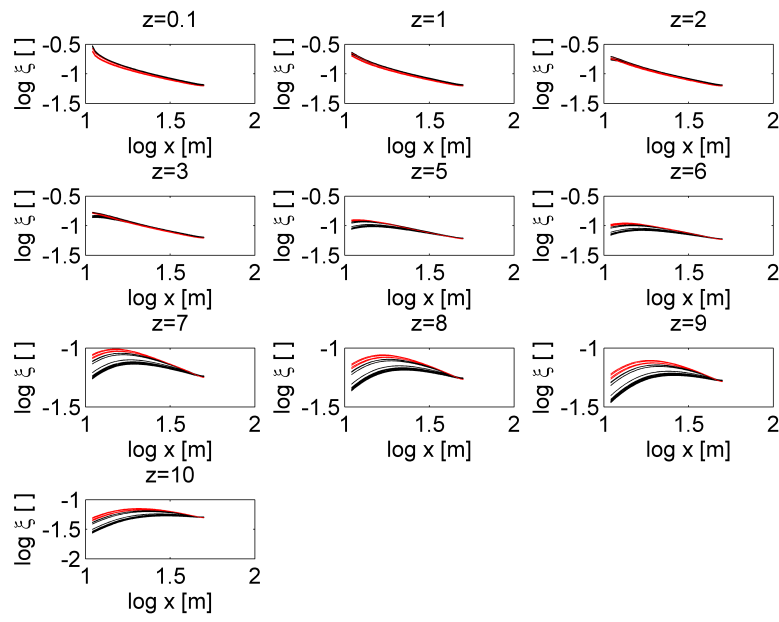
Fig. 11 Same as Figure 10. In red, the concentration profiles that show recirculation.
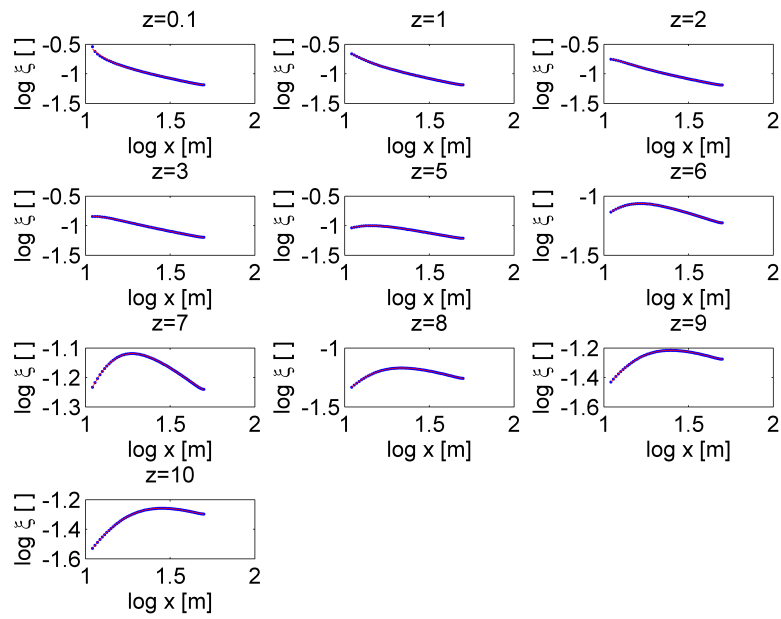
Fig. 12 Same as Figure (11). The blue dots represent the average value of the concentration profiles in Figure (11), excluding those that manifest recirculation.
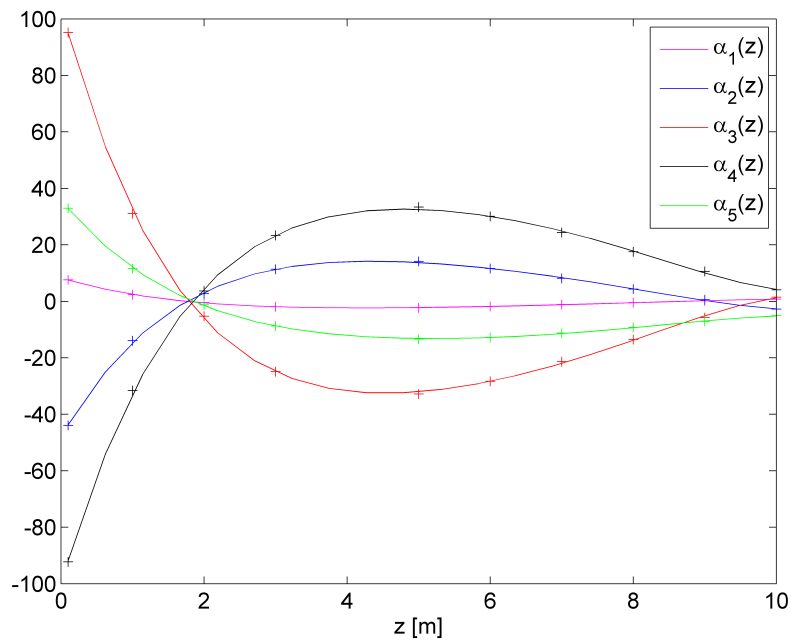
Fig. 13 The coefficients α_k (indicated by points with a + sign) represent the coefficients of the 4th order polynomial interpolation between the log of the horizontal distance from the source and the log of the normalized concentration for the case $b = 6$. The colored solid lines represent the 5th order polynomials interpolating the coefficients $\alpha_k(z)$ as a function of the elevation z, in the range from 1 m to 10 m. In 1, we summarize the coefficients of this interpolation for different values of the seepage length b.